



Characterizing the measurement resolution and measurement bias of Sampling Moiré

Frédéric Sur, Benoît Blaysat, Michel Grédiac

► To cite this version:

Frédéric Sur, Benoît Blaysat, Michel Grédiac. Characterizing the measurement resolution and measurement bias of Sampling Moiré. *Optics and Lasers in Engineering*, 2024, 177, pp.108130. 10.1016/j.optlaseng.2024.108130 . hal-04497407

HAL Id: hal-04497407

<https://hal.science/hal-04497407>

Submitted on 10 Mar 2024

HAL is a multi-disciplinary open access archive for the deposit and dissemination of scientific research documents, whether they are published or not. The documents may come from teaching and research institutions in France or abroad, or from public or private research centers.

L'archive ouverte pluridisciplinaire **HAL**, est destinée au dépôt et à la diffusion de documents scientifiques de niveau recherche, publiés ou non, émanant des établissements d'enseignement et de recherche français ou étrangers, des laboratoires publics ou privés.

Characterizing the measurement resolution and measurement bias of Sampling Moiré

Frédéric Sur,^{*} Benoît Blaysat,[†] Michel Grédiac[†]

Abstract

Sampling moiré is a spatial fringe pattern analysis method which can be used to retrieve displacement fields on the surface of deformed specimens marked by a periodic pattern. We prove that, under mild assumptions, Sampling Moiré (SM) is equivalent to another full-field method, namely the Localized Spectrum Analysis (LSA). The prospects opened up by this result concern two metrological indicators, namely the measurement bias (the retrieved displacement being affected by a systematic error) and the measurement resolution (limited by the propagation of sensor noise to displacement maps). Previous studies on LSA yield predictive formulas for measurement bias and displacement resolution. These formulas are adapted here to the case of SM. Relevant numerical studies enable us to assess to what extent those predictive formulas are satisfied, interpolation performed in SM and not in LSA affecting the quality of the final result.

Keywords: sampling moiré, localized spectrum analysis, Fourier methods, metrological performance.

This is the author-manuscript version of

F. Sur, B. Blaysat, M. Grédiac. Characterizing the measurement resolution and measurement bias of Sampling Moiré. *Optics and Lasers in Engineering*, vol. 177, p. 108130, 2024.

DOI: 10.1016/j.optlaseng.2024.108130

^{*}LORIA, UMR 7503, Université de Lorraine, CNRS, INRIA, Nancy, France

[†]Institut Pascal, UMR 6602, Université Clermont Auvergne, CNRS, Clermont Auvergne INP, Clermont-Ferrand, France

1 Introduction

Measuring displacement and strain fields on the surface of flat specimens under test is a major issue in experimental mechanics. Digital Image Correlation (DIC) [31, 40] is undoubtedly the most common technique, but standard versions rely on random patterns, and the metrological performance is not optimal in this case [2, 11]. Employing periodic patterns such as grids or checkerboards gives better performance [14]. However, classic versions of DIC generally fail to converge because of the multiplicity of the local minima of the function to be minimized [40]. Spectral methods are commonly used instead of DIC to process images of periodic patterns. These methods share the same feature: the fact that phase distributions must be extracted from images, the phase difference between deformed and reference distributions (denoted by ϕ^{def} and ϕ^{ref} , respectively) being, at first approximation, proportional to the sought displacement u through the following equation:

$$u = -\frac{P}{2\pi} (\phi^{\text{def}} - \phi^{\text{ref}}) \quad (1)$$

where P is the period of the periodic pattern, also known as pattern pitch.

A broad literature deals with this problem, and different spectral techniques have been proposed to extract phase distributions from images of periodic patterns. Assuming that the magnitude of the strain remains small, the straight lines (for a grid) or the alignment of tiny squares (for a checkerboard) forming the pattern are only slightly affected by deformation. The periodic signal describing the gray level distribution can therefore be considered as a spatial carrier with a constant period of P , this signal being locally modulated by deformation. In this case, the most frequently used techniques to retrieve the phase distributions are the Geometric Phase Analysis (GPA) [19, 20], its windowed version (WGPA) [6, 7], the Localized Spectrum Analysis (LSA) [12, 15] and Sampling Moiré (SM) [36, 38, 50]. The link between the first three is discussed in [16]. For instance, it is shown that LSA can be considered a particular WGPA case. More general approaches have also been developed in the optical metrology community to process images of fringes [25, 41]. They are more general in the sense that the period P of the pattern may significantly spatially change, the case of a constant value becoming a particular case. This leads to a set of techniques such as the so-called Fourier transform method [46], the windowed Fourier filtering [22], the windowed Fourier ridge method (WFR) [23], the spatial carrier phase-shifting method [32], and SM again. The link between these latter techniques is discussed in [25]. In particular, SM is shown to be a particular case of WFR [26]. The main difference is that the Gaussian window employed with the latter is substituted by a triangular or a cubic window with the former.

In this context, the aim of the present contribution is first to demonstrate in another way the same result as in [25, 26] by relying on the fact that interpolation like that performed in SM can be considered as a convolution with a suitable kernel, as explained in detail in [27]. The present paper focuses on periodic patterns such as 2D grids modulated by small deformations. This is a case where WFRM is equivalent to LSA, with a spatially constant period of the carrier. Then, we take advantage of the link between SM and LSA to adapt to SM formulas quantifying some metrological parameters of LSA in the case of 2D grids and discuss to what extent those formulas apply to SM, since interpolation of raw data performed in SM does not appear in LSA.

The rest of the paper is organized as follows. Section 2 is a careful analysis of SM. Section 3 demonstrates a result linking SM and LSA similarly to WFR, by considering interpolation as a convolution. Section 4 uses this result to present predictive formulas for measurement resolution and bias in SM, in the case of 2D grids deformed through small strain fields. Numerical assessments are discussed in Section 5.

2 A primer on sampling moiré

The goal of this section is to present a careful analysis of SM.

2.1 From one 2D grid to two 1D fringe patterns

In SM, a 2D grid pattern is first reduced to two independent 1D fringe patterns by applying a moving average filter w_{MA} , which eliminates the periodic pattern along one of the axes. Assuming the period of the grid is an integer, a popular choice for this filter is a centered moving average [30, 36]: if the pattern pitch P is odd, the length of w is P and its coefficients are $(w_{\text{MA}})_k = 1/P$ for $|k| \leq (P-1)/2$, and, if P is even, the length is $P+1$ and the coefficients are $(w_{\text{MA}})_k = 1/P$ if $|k| \leq P/2 - 1$ and $(w_{\text{MA}})_k = 1/(2P)$ if $|k| = P/2$. It should be noted that, with even values of P , using a non-centered moving average would give a localization error of half a pixel. In the following, we note $w_{\text{MA}}^{\text{odd}}$ and $w_{\text{MA}}^{\text{even}}$ these moving average kernels, respectively. Grids with non-integer pitches may, in practice, still be processed with these kernels, as discussed in Section 5.

In practice, 2D grids are generally not aligned with the rows of pixels of the camera sensor. Moving average filtering must therefore be performed using a filter defined over an oblique window, as in [28, 50]. This additional operation induces some errors in the grid images. However, the impact on the displacement field eventually retrieved by SM is challenging to assess, so we stick here with grids aligned with the horizontal and vertical axes.

Without loss of generality, we now consider the signal obtained as the convolution of the 2D grid by w_{MA} along one of the principal directions of the grid. This signal is a 1D fringe pattern that can be analyzed in one direction. For simplicity, we focus in the remainder of this section on analyzing a unidimensional fringe pattern.

Such a pattern is modeled by the following equation:

$$s(x) = a(x) + b(x) \cos(2\pi f_P x + \phi_{\text{true}}(x)) \quad (2)$$

where s , a , and b are the fringe pattern intensity, the background intensity, and the fringe amplitude, respectively. The carrier frequency is denoted by f_P . It is equal to the inverse of the fringe pitch P . Both background and fringe intensity may smoothly vary across the imaged field, but they are considered as constant values in the following calculation. The unknown phase to be determined is ϕ_{true} . To alleviate the notations, we skip $a(x)$ and $b(x)$ in the following.

2.2 Successive downsamplings and interpolation

A sampling pitch S is first chosen. Except in [49] where $S = P/2$ is used, its value is generally lower than and close to P . The periodic signal s is therefore downsampled every S pixels.

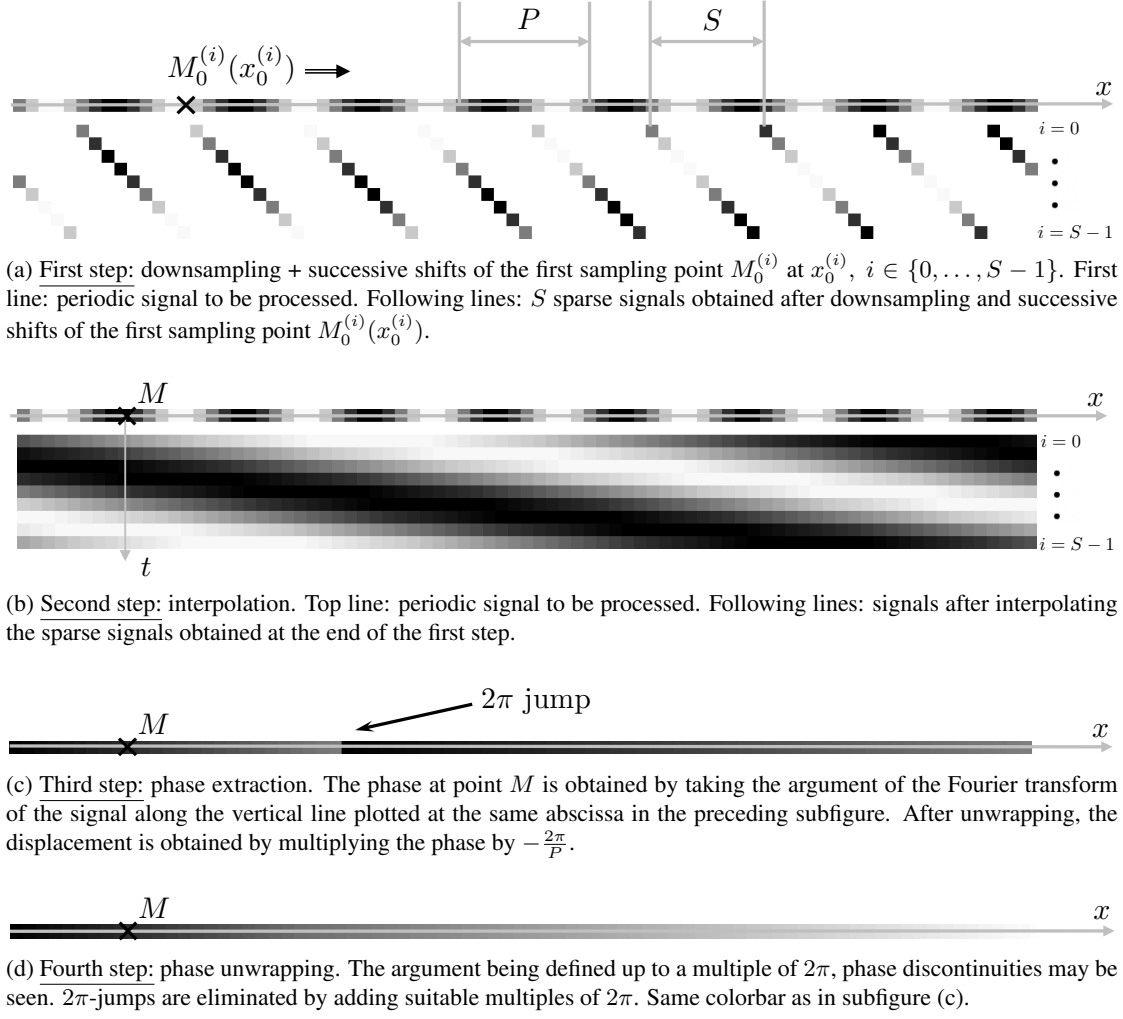


Figure 1: Principle of sampling moiré.

An important feature is that this downsampling procedure is repeated S times, the abscissa $x_0^{(i)}$, $i \in \{0, \dots, S-1\}$ of the first sampling point, denoted here by $M_0^{(i)}(x_0^{(i)})$, increasing by one pixel from one case to another, thus $x_0^{(i)} \in \{0, \dots, S-1\}$ [px]. This results in S different sparse signals denoted by $s^{(i)}$, $i \in \{0, \dots, S-1\}$, such that:

$$\begin{cases} s^{(i)}(x_0^{(i)} + kS) = s(x_0^{(i)} + kS) & \forall k \in \mathbb{Z}, i \in \{0, \dots, S-1\} \\ s^{(i)}(x) = 0 & \text{otherwise} \end{cases} \quad (3)$$

This first step of the procedure is illustrated in Figure 1-a.

The second step is to assign a value at the pixels where no information is available in the sparse signals $s^{(i)}$, $i \in \{0, \dots, S-1\}$. They are therefore completed to form i different signals

denoted by $\tilde{s}^{(i)}$, $i \in \{0, \dots, S-1\}$. These signals have the same size as the initial one s . They are such that for any pixel x lying between the $x_0^{(i)} + kS$ sampling points, $i \in \{0, \dots, S-1\}$, the value assigned to $\tilde{s}^{(i)}(x)$ is obtained by interpolation between the sampling points. As discussed in Section 3 below, various types of interpolation can be used for this. This second step is illustrated in Figure 1-b.

2.3 Calculation of the apparent frequency of the sampled fringes

Since the sampling pitch S is close to the fringe pitch P , the Nyquist condition is not met. Indeed, the sampling frequency $f_S = 1/S$ is lower than twice the signal frequency $2f_P = 2/P$. The fringe patterns corresponding to the interpolated $\tilde{s}^{(i)}$, $i \in \{0, \dots, S-1\}$, are called *moiré fringe patterns* in the papers dealing with SM, see [30, 47] for instance. These fringes have an apparent frequency that is much lower than the one of the initial pattern s , as can be seen in Figure 1-b. The objective of the following calculations is to show that the value of this frequency is $|f_P - f_S|$.

First, bearing in mind that the original signal s is modeled with a cosine function (see Equation 2), it is worth noting that the following equality holds for any $m \in \mathbb{Z}$ and for any sampling point $x = x_0^{(i)} + kS$:

$$\cos\left((2\pi(f_P + mf_S)x + \phi_{\text{true}}(x) - 2\pi mf_S x_0^{(i)})\right) = \cos(2\pi f_P x + \phi_{\text{true}}(x)) \quad (4)$$

Indeed, if $x = x_0^{(i)} + kS$ in the left-hand member of Equation 4, we have

$$\begin{aligned} & \cos\left((2\pi(f_P + mf_S)(x_0^{(i)} + kS) + \phi_{\text{true}}(x_0^{(i)} + kS) - 2\pi mf_S x_0^{(i)})\right) \\ &= \cos\left(2\pi f_P(x_0^{(i)} + kS) + 2\pi mf_S kS + \phi_{\text{true}}(x_0^{(i)} + kS)\right) \\ &= \cos\left(2\pi f_P(x_0^{(i)} + kS) + \phi_{\text{true}}(x_0^{(i)} + kS)\right) \end{aligned} \quad (5)$$

since $f_S S = 1$ and the cosine function is 2π -periodic.

This means that, by definition of $s^{(i)}$ (see Equation 3), for every $m \in \mathbb{Z}$, the function $s_m^{(i)}$ defined for any value of x by

$$s_m^{(i)}(x) = \cos\left((2\pi(f_P + mf_S)x + \phi_{\text{true}}(x) - 2\pi mf_S x_0^{(i)})\right) \quad (6)$$

are indistinguishable from $s^{(i)}(x)$ at the sampling points $x = x_0^{(i)} + kS$. In sampling theory [29], the $s_m^{(i)}$ functions are called *aliases*. Interpolation gives an approximation of one of these aliases. We will see now that interpolation retrieves an approximation of the alias with the smallest frequency.

According to the Shannon-Nyquist interpolation theorem [29], if the Nyquist condition is satisfied, band-limited signals whose spectra are supported by the interval $(-f_S/2, f_S/2)$ are perfectly reconstructed from their samples by *i*- first multiplying the discrete Fourier transform of the sampled signal by a Heaviside step of width $f_S/2$, and *ii*- then taking the inverse Fourier

transform of the result. Interpolation kernels are thus designed so that their Fourier transform approximates this Heaviside step. However, the Nyquist condition is not satisfied here. Consequently, the $s^{(i)}$ functions have frequency components outside the $(-f_S/2, f_S/2)$ interval which are removed by interpolation. Equation 6 shows that interpolation retrieves an approximation of one of the aliases $s_m^{(i)}$ of frequency $|f_P + mf_S|$. Only one of the values of $|f_P + mf_S|$ with $m \in \mathbb{Z}$ lies in $(-f_S/2, f_S/2)$, namely the smallest value. One can see that the smallest value of $|f_P + mf_S|$ when $m \in \mathbb{Z}$ is the carrier frequency f_P if and only if $f_S > 2f_P$. In other words, when the Nyquist condition is satisfied, downsampling gives an interpolated signal with the same frequency as the original one. In SM, the sampling pitch S is chosen to be approximately equal to the fringe pitch P , so this condition is not satisfied, as mentioned above. Consequently, in SM, the sampled signal has a frequency equal to $|f_P - f_S|$ since the smallest value of $|f_P + mf_S|$ is attained for $m = -1$.

We can conclude that the interpolation of each $s^{(i)}$ (denoted by $\tilde{s}^{(i)}$) is approximately $s_m^{(i)}$ with $m = -1$, that is,

$$\tilde{s}^{(i)}(x) \simeq \cos \left((2\pi(f_P - f_S)x + \phi_{\text{true}}(x) + 2\pi f_S x_0^{(i)}) \right) \quad (7)$$

This approximation can potentially have a detrimental effect on the displacement returned by SM. This is not the case with temporal phase shifting (as long as the phase shift is well-controlled in practice), for which complete fringe maps are obtained without interpolation. It is claimed in [47] that interpolation has high accuracy because the frequency $|f_P - f_S|$ is usually very small, the moiré fringes being thus easier to interpolate than the original fringe pattern since their frequency is much lower. This accuracy is quantified in [37] in the case of linear interpolation, and a phase compensation method is also proposed to correct the systematic estimation bias. We shall return to this point in Section 3.3.

2.4 Retrieving the phase distribution

Finally, in SM, the phase $2\pi(f_P - f_S)x + \phi_{\text{true}}(x)$ is retrieved as the argument of the discrete Fourier transform taken at frequency f_S as follows:

$$\sum_{i=0}^{S-1} \tilde{s}^{(i)}(x) e^{-2j\pi f_S x_0^{(i)}} \quad (8)$$

where j is the imaginary unit.

Indeed, by replacing $\tilde{s}^{(i)}$ by the approximated value given by Equation 7, Equation 8 reads with Euler's formula:

$$\begin{aligned} & \frac{1}{2} \sum_{i=0}^{S-1} \left(e^{j(2\pi(f_P - f_S)x + \phi_{\text{true}}(x) + 2\pi f_S x_0^{(i)})} + e^{-j(2\pi(f_P - f_S)x + \phi_{\text{true}}(x) + 2\pi f_S x_0^{(i)})} \right) e^{-2j\pi f_S x_0^{(i)}} \\ &= \frac{S}{2} e^{j(2\pi(f_P - f_S)x + \phi_{\text{true}}(x))} + e^{-j(2\pi(f_P - f_S)x + \phi_{\text{true}}(x))} \sum_{i=0}^{S-1} e^{-4j\pi f_S x_0^{(i)}} \quad (9) \\ &= \frac{S}{2} e^{j(2\pi(f_P - f_S)x + \phi_{\text{true}}(x))} \end{aligned}$$

since $\sum_{i=0}^{S-1} e^{-4j\pi f_S x_0^{(i)}} = 0$ when $f_S = 1/S$ and $x_0^{(i)} \in \{0, \dots, S-1\}$. Taking the argument of Equation 8 thus gives the phase estimated by SM:

$$\phi_{\text{SM}}(x) = 2\pi(f_P - f_S)x + \phi_{\text{true}}(x). \quad (10)$$

This third step is illustrated in Figure 1-c. Note that $\phi_{\text{SM}}(x)$ is wrapped if the displacement spans an interval greater than one period P , as illustrated in the example in Figure 1-c where one phase jump is observed. Hence, the fourth step consists in unwrapping the phase distribution by adding multiples of 2π . Different algorithms are available to perform this task, see [9, 18, 21]. This fourth step is illustrated in Figure 1-d. A continuous phase distribution is finally obtained.

2.5 Accounting for the displacement between the coordinate systems of the reference and deformed configurations

The raw phase $\phi_{\text{SM}}(x)$ retrieved by SM is different from $\phi_{\text{true}}(x)$, which eventually gives the sought displacement by using Equation 1, as in the usual SM method. The difference between $\phi_{\text{SM}}(x)$ and $\phi_{\text{true}}(x)$ is equal to $2\pi(f_P - f_S)x$ according to Equation 10. It is the same for both the reference and the deformed configurations, thus

$$\begin{cases} \phi_{\text{SM}}^{\text{ref}}(x) = 2\pi(f_P - f_S)x + \phi_{\text{true}}^{\text{ref}}(x) \\ \phi_{\text{SM}}^{\text{def}}(x) = 2\pi(f_P - f_S)x + \phi_{\text{true}}^{\text{def}}(x) \end{cases} \quad (11)$$

It means that deducing the displacement by merely subtracting pixel by pixel the phases given by SM for the deformed and reference configurations gives the phase difference, which is proportional to the displacement according to Equation 1, $2\pi(f_P - f_S)x$ vanishing after this subtraction. However, as discussed for instance in [15], subtracting the phases at the same physical point instead of pixel by pixel improves the quality of the displacement and strain fields eventually returned by spectral techniques. Indeed, this procedure enables us to eliminate, within certain limits, local defects, which always impair periodic patterns, and thus the displacement and strain fields returned by the measuring technique. This gives in the 1D case:

$$u(x) = \frac{-P}{2\pi}(\phi_{\text{true}}^{\text{def}}(x + u(x)) - \phi_{\text{true}}^{\text{ref}}(x)) \quad (12)$$

In this case, the sought displacement u appears in both the left- and the right-hand sides of the preceding equality. Displacement u is therefore found using a fixed-point algorithm, as explained in [15] for instance. Hence, Equation 11 above reads as follows

$$\begin{cases} \phi_{\text{SM}}^{\text{ref}}(x) = 2\pi(f_P - f_S)x + \phi_{\text{true}}^{\text{ref}}(x) \\ \phi_{\text{SM}}^{\text{def}}(x + u(x)) = 2\pi(f_P - f_S)(x + u(x)) + \phi_{\text{true}}^{\text{def}}(x + u(x)) \end{cases} \quad (13)$$

The consequence is that $2\pi(f_P - f_S)x$ shall be subtracted from the phase distributions $\phi_{\text{SM}}^{\text{ref}}$ and $\phi_{\text{SM}}^{\text{def}}$ returned by SM before resolving Equation 12, the quantity $2\pi(f_P - f_S)(x + u(x)) - 2\pi(f_P - f_S)x$ no longer vanishing from $\phi_{\text{SM}}^{\text{def}}(x + u(x)) - \phi_{\text{SM}}^{\text{ref}}(x)$ if directly calculating the displacement with $\phi_{\text{SM}}^{\text{def}}$ and $\phi_{\text{SM}}^{\text{ref}}$ with the fixed-point algorithm in Equation 12.

3 Link between SM and LSA

In this section, a finer analysis shows that SM and LSA are equivalent windowed Fourier methods which mainly differ in the choice of the analysis window.

3.1 Interpolation as a convolution

An important remark is that numerous interpolation schemes can be described as a convolution with a kernel denoted here by w_{interp} , see [8, 27] for instance. Sampled values on a discrete grid of each $s^{(i)}$ being available, the interpolation of each of them (thus $\tilde{s}^{(i)}$) writes as follows:

$$\tilde{s}^{(i)}(x) = \sum_{n \in \mathbb{Z}} s^{(i)}(n) w_{\text{interp}}(x - n) \quad (14)$$

for any $x \in \mathbb{R}$.

For example and as explained in [27], linear interpolation corresponds to the following triangular kernel:

$$w_{\text{interp}}^{\text{lin}}(x) = \begin{cases} \alpha \left(1 - \frac{|x|}{S}\right) & \text{for } |x| \in [0, S] \\ 0 & \text{otherwise} \end{cases} \quad (15)$$

with $\alpha = 1$, such that $w_{\text{interp}}^{\text{lin}}(0) = 1$. See Figure 2.

Cubic interpolation corresponds to the following cubic kernel:

$$w_{\text{interp}}^{\text{cub}}(x) = \begin{cases} \beta \left(\frac{3}{2} \frac{|x|^3}{S^3} - \frac{5}{2} \frac{|x|^3}{S^3} + 1 \right) & \text{for } |x| \in [0, S] \\ \beta \left(-\frac{1}{2} \frac{|x|^3}{S^3} + \frac{5}{2} \frac{|x|^2}{S^2} - 4 \frac{|x|}{S} + 2 \right) & \text{for } |x| \in [S, 2S] \\ 0 & \text{otherwise} \end{cases} \quad (16)$$

with $\beta = 1$. Kernels corresponding to other types of interpolations, such as cubic spline and nearest neighbor interpolation, are given in [27]. In all cases, interpolation kernels are (most usually) even functions.

Linear and cubic-spline interpolations are used in [36, 48], respectively, but it seems that no exhaustive study on the impact of the nature of the interpolation is available in the SM literature except for linear intensity interpolation in [37].

Any interpolated moiré fringe pattern $\tilde{s}^{(i)}$ writes as follows for $i \in \{0, \dots, S-1\}$:

$$\tilde{s}^{(i)}(x) = \sum_{k \in \mathbb{Z}} s^{(i)}(x_0^{(i)} + kS) w_{\text{interp}}(x - x_0^{(i)} - kS) \quad (17)$$

In practice, the size of the kernel support (thus the sum in Equation 17) is finite and depends on the sampling pitch S . For instance, the triangular kernel above has a support length of $2S$ ($k \in \{-1, 0, 1\}$ in Equation 17) while this support length is equal to $4S$ with the cubic one ($k \in \{-2, -1, 0, 1, 2\}$).

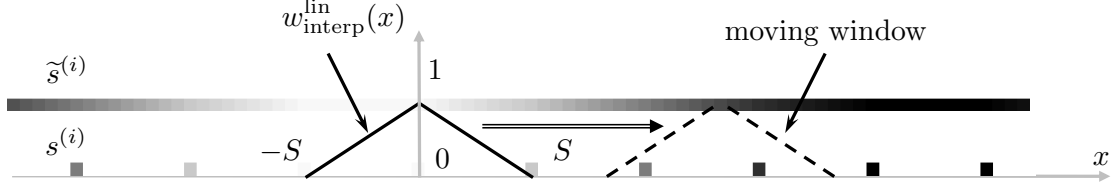


Figure 2: Triangular moving window $w_{\text{interp}}^{\text{lin}}$ used as a kernel to perform linear interpolation by convolution. Bottom: typical sparse signal $s^{(i)}$ obtained after downsampling the original signal s . Top: gray level distribution $\tilde{s}^{(i)}$ obtained after convolution, by the triangular kernel, of the sparse signal $s^{(i)}$ depicted at the bottom.

3.2 Fourier analysis of interpolated moiré fringe pattern

By definition of $s^{(i)}$, we have $s^{(i)}(x_0^{(i)} + kS) = s(x_0^{(i)} + kS)$. Plugging Equation 17 into the Fourier transform given by Equation 8 thus gives:

$$\sum_{i=0}^{S-1} \sum_{k \in \mathbb{Z}} s(x_0^{(i)} + kS) w_{\text{interp}}(x - x_0^{(i)} - kS) e^{-2j\pi f_S x_0^{(i)}} \quad (18)$$

which also writes as follows:

$$\sum_{x_0^{(i)}=0}^{S-1} \sum_{k \in \mathbb{Z}} s(x_0^{(i)} + kS) w_{\text{interp}}(x - x_0^{(i)} - kS) e^{-2j\pi f_S (x_0^{(i)} + kS)} \quad (19)$$

since $f_S S = 1$ and $x_0^{(i)}$ spans the same interval as i .

The set of all $x_0^{(i)} + kS$ for all integer values $0 \leq x_0^{(i)} < S$ and $k \in \mathbb{Z}$ being simply \mathbb{Z} , this latter expression further simplifies into:

$$\sum_{\xi \in \mathbb{Z}} s(\xi) w_{\text{interp}}(\xi - x) e^{-2j\pi f_S \xi} \quad (20)$$

since $w_{\text{interp}}(x - \xi) = w_{\text{interp}}(\xi - x)$, the interpolation kernel being symmetric.

This is simply the discrete windowed Fourier transform (WFT) of the signal s at the frequency f_S , except that the interpolation kernel w_{interp} does not integrate to 1 as the kernels used in WFT. It should be noted that this does not affect the argument of Equation 20 (which is a simple rewriting of Equation 8) to obtain ϕ_{SM} , namely the phase estimated through SM. In other terms, the value of α (resp. β) in Equation 15 (resp. 16) does not change the phase estimation by SM.

3.3 Comparison between SM and LSA

SM basically relies on the fact that the approximation given by the interpolation in Equation 7 is accurate enough to deduce the phase ϕ_{true} by Fourier transform. Taking the equality as granted

permits to obtain the estimation: $\phi_{\text{SM}}(x) = 2\pi(f_P - f_S)x + \phi_{\text{true}}(x)$; and ultimately an estimation of $\phi_{\text{true}}(x)$ as explained in Section 2.5.

A demonstration similar to that of Section 2 is already available in [26], and numerical experiments in [35]. In [26], SM is shown to be a special windowed Fourier ridge (WFR) algorithm, where the ridge frequency is not sought as the maximum in the amplitude spectrum of the signal but is set to the sampling frequency. The authors of [26] analyze the estimation error caused by the mismatch between both frequencies and conclude that a locally linear phase gives an error-free estimation. This explains why SM can be used even with a rough estimation of the fringe pitch giving a small difference between f_P and f_S .

For its part, LSA [15] simply consists in taking the argument of the windowed Fourier transform:

$$\sum_{\xi \in \mathbb{Z}} s(\xi) w(\xi - x) e^{-2j\pi f \xi} \quad (21)$$

where $f = f_P$ is the frequency of the carrier fringe, and w is usually a Gaussian analysis window, noted w_{Gauss} here. Other types of windows can be used, but it has been shown in [45] that a Gaussian window leads to the best trade-off between various constraints.

Noting

$$\phi_{\text{LSA}}^f(x) = \arg \left(\sum_{\xi \in \mathbb{Z}} s(\xi) w_{\text{interp}}(\xi - x) e^{-2j\pi f \xi} \right), \quad (22)$$

then $\phi_{\text{LSA}}^{f_P}(x)$ is the classic LSA estimation with w_{interp} instead of w_{Gauss} , and $\phi_{\text{LSA}}^{f_S}(x) = \phi_{\text{SM}}(x)$ if Equation 7 is actually an equality instead of an approximation.

Let us write a first-order expansion of the phase around x as

$$\phi_{\text{true}}(x + \xi) = \phi_{\text{true}}(x) + \phi'_{\text{true}}(x)\xi + \phi_x(\xi) \quad (23)$$

with ϕ'_{true} the derivative of ϕ_{true} . The complex signal s writes $s(\xi) = e^{j(2\pi f_P \xi + \phi_{\text{true}}(\xi))}$, thus:

$$\phi_{\text{LSA}}^f(x) = \arg \left(\sum_{\xi \in \mathbb{Z}} w_{\text{interp}}(\xi - x) e^{j(2\pi f_P \xi + \phi_{\text{true}}(\xi))} e^{-2j\pi f \xi} \right) \quad (24)$$

$$= \arg \left(\sum_{\xi \in \mathbb{Z}} w_{\text{interp}}(\xi) e^{j(2\pi(f_P - f)(x + \xi) + \phi_{\text{true}}(x + \xi))} \right) \quad (25)$$

$$= \arg \left(e^{j(2\pi(f_P - f)x + \phi_{\text{true}}(x))} \sum_{\xi \in \mathbb{Z}} w_{\text{interp}}(\xi) e^{j(2\pi(f_P - f) + \phi'_{\text{true}}(x))\xi} e^{j\phi_x(\xi)} \right) \quad (26)$$

$$= 2\pi(f_P - f)x + \phi_{\text{true}}(x) + \widetilde{\phi_{\text{true}}}(x) \quad (27)$$

where $\widetilde{\phi_{\text{true}}}(x) = \arg \left(\sum_{\xi \in \mathbb{Z}} w_{\text{interp}}(\xi) e^{j(2\pi(f_P - f) + \phi'_{\text{true}}(x))\xi} e^{j\phi_x(\xi)} \right)$.

When ϕ_x in Equation 23 is a null function (i.e., when ϕ_{true} is locally linear around x), one has $\widetilde{\phi_{\text{true}}} = 0$ since, for any real value ψ , $\sum_{\xi \in \mathbb{Z}} w_{\text{interp}}(\xi) e^{j\psi\xi}$ is a real number as the value of the discrete Fourier transform of a real even function.

Consequently, with a locally linear phase, Equations 27 and 10 give:

$$\phi_{\text{LSA}}^{f_S}(x) = \phi_{\text{SM}}(x) \quad (28)$$

which is another demonstration of the result in [26]. In addition, substituting f by f_P in Equation 27 shows that the standard LSA method gives in this case:

$$\phi_{\text{LSA}}^{f_P}(x) = \phi_{\text{true}}(x) \quad (29)$$

Consequently,

$$\phi_{\text{SM}}(x) = 2\pi(f_P - f_S) + \phi_{\text{LSA}}^{f_P}(x) \quad (30)$$

under the locally-linear phase assumption.

Besides, in the same spirit as in [26], it can be noted that LSA is a WFR method where the ridge frequency is set to the pattern frequency value, which is the maximum in the amplitude spectrum of the signal. From this point of view, the three methods (SM, WFR, LSA) are basically the same since they rely on phase estimation from a quasi-periodic pattern with windowed Fourier transform. However, SM introduces an additional bias when the sampling frequency f_S differs from the pattern frequency f_P and the phase is not locally linear (which is the case in practice), as the phase is no longer estimated from the maximum of the amplitude spectrum, contrary to WFR and LSA.

3.4 Back to 2D grids

The preceding mathematical derivation was achieved with 1D fringe patterns along the x -axis. As Section 2.1 explains, the input signal is a 2D grid pattern convolved with a moving average kernel w_{MA} along the y -axis. Let us denote by $\mathfrak{s}(x, y)$ the 2D grid pattern. The fringe pattern along the x -axis thus reads as follows:

$$s(x, y) = \sum_{\eta \in \mathbb{Z}} \mathfrak{s}(x, \eta) w_{\text{MA}}(y - \eta) \quad (31)$$

where w_{MA} is the window corresponding to the centered moving average discussed in Section 2.1. As explained above, for any value of y , $s(x, y)$ is then processed by SM.

Processing the grid image \mathfrak{s} with SM thus consists in estimating $\phi_{\text{SM}}(x, y)$ at any (x, y) by taking the argument of

$$\begin{aligned} & \sum_{\xi \in \mathbb{Z}} \sum_{\eta \in \mathbb{Z}} \mathfrak{s}(\xi, \eta) w_{\text{MA}}(y - \eta) w_{\text{interp}}(x - \xi) e^{-2j\pi f_S \xi} \\ &= \sum_{(\xi, \eta) \in \mathbb{Z}^2} \mathfrak{s}(\xi, \eta) w_{\text{SM}}(x - \xi, y - \eta) e^{-2j\pi f_S \xi} \end{aligned} \quad (32)$$

where

$$w_{\text{SM}}(x, y) = w_{\text{interp}}(x) w_{\text{MA}}(y) \quad (33)$$

is the separable filter obtained as the tensor product of the 1D interpolation kernel w_{interp} along the x -axis and of the 1D moving average kernel w_{MA} along the y -axis.

	SM	LSA
interpolation of raw data	yes	no
kernel	$w_{\text{SM}}(x, y) = w_{\text{interp}}(x)w_{\text{MA}}(y)$	$w_{\text{LSA}}(x, y) = w_{\text{Gauss}}(x, y)$ as an optimal window [45]
size of the kernel	stepwisely changes	continuously changes

Table 1: Main differences between SM and LSA.

4 Insights on SM based on the equivalence with LSA

The preceding section shows that SM and LSA are equivalent under the hypothesis of locally linear phase maps, cf. Equation 30. Both methods require, however, practical choices that explain differences in the numerical estimation of displacements and strain maps. They are explained in Section 4.1

As mentioned earlier, the fundamental assumption of SM is that the interpolation is accurate enough so that Equation 7 is strictly (and not only approximately) satisfied. Regarding LSA, we can go beyond this assumption and show that a systematic measurement bias is inherent to the method. The remainder of this section is dedicated to the estimation of the measurement bias of SM (Section 4.2) and its displacement resolution (Section 4.3) from earlier results on LSA. To the best of our knowledge, the predictive formulas obtained in this section are not available in the SM literature. Concerning the noise transfer, only numerical comparisons between SM or other Fourier methods are given in [35].

4.1 Practical differences between SM and LSA

First, the kernels used in SM and LSA differ. Concerning LSA, differences can be seen depending on the analysis kernel, the Gaussian kernel presenting the best trade-off between different constraints [45]. The choice of the interpolation scheme certainly plays a role that is, to the best of our knowledge, not analyzed in the framework of SM. It should be noted that Gaussian kernels are also used in WFR [24].

Second, while the size of Gaussian windows used in LSA and WFR can continuously change, both the triangular and the cubic windows used in SM span a fixed interval ($[-S S]$ and $[-2S 2S]$, respectively), which can only be set by stepwisely changing the sampling period S . The same remark holds for the moving average filter w_P removing the periodic component.

Table 1 gathers the main differences between SM and LSA.

4.2 Measurement bias

It is shown in [44] that the phase estimated with LSA is not exactly the true phase ϕ_{true} , as assumed in Equation 29, but the convolution of ϕ_{true} and the analysis kernel. It is therefore

affected by a systematic bias, which manifests itself by a blur of the displacement and mainly the strain maps. This property is valid under the small strain assumption (basically, under small phase derivatives), which is a less restrictive assumption than affine phases, as required by SM.

Let us assume that Equation 30, which holds rigorously under the locally affine phase assumption, permits to transfer this result to the phase estimation by SM. The kernel w_{SM} defined in Equation 33 must be normalized such that it integrates to 1 from the remark after Equation 20 (a normalized kernel is indeed required so that the following equation holds true), which amounts to choosing the right values for α and β in Equations 15 and 16. This does not change ϕ_{SM} as explained just after Equation 20. Thus

$$\phi_{\text{SM}} = 2\pi(f_P - f_S) + \bar{w}_{\text{SM}} * \phi_{\text{true}} \quad (34)$$

where $*$ denotes the convolution product, and \bar{w}_{SM} is $w_{\text{SM}} / \int w_{\text{SM}}$.

As a sanity check, it can be noted that, in the case of a locally-affine phase, Equation 34 boils down to Equation 10. Indeed, the convolution of any affine function by an odd kernel is still the original affine function,

Therefore, when the phase difference is performed pixel by pixel to obtain the displacement (see Equation 1), the displacement obtained by SM is not directly the true displacement, but the true displacement convolved by w_{SM} . Thus

$$u_{\text{SM}} = \bar{w}_{\text{SM}} * u_{\text{true}} \quad (35)$$

When the phase difference is calculated at the same physical point, a fixed-point algorithm deduces u from the phases (see Equation 12), which induces a non-linear relation between displacement and phase change. However, it has been observed in the case of Gaussian kernels that, at first approximation, Equation 35 remains valid in this case. From a practical point of view, the consequence of this property is the same for SM and LSA, namely, the displacement and strain maps are blurred by this convolution. In a similar way to LSA [10, 13] this property also paves the way for further studies on deconvolution of the phase maps to enhance the spatial resolution of SM, the spatial resolution representing the lowest distance between independent measurements in a displacement or strain map for a given measurement bias [52]. The difference with LSA would be the nature of the kernel to be used (rectangular-triangular or rectangular-cubic instead of Gaussian). Examining these points is, however, out of the scope of the present study.

An alternative interpretation of the preceding remark can be drawn by comparing SM with the way fringes are processed with temporal phase shifting in interferometry. Temporal phase shifting consists in slightly changing the difference in the optical path length between two laser beams which are combined to form a fringe pattern [5, 17, 39]. This phase shift can be obtained by moving a mirror or a grating, or by tilting a glass plate, for instance, these optical components being parts of the interferometric setup under consideration. The idea is to apply this shift N times, so that the difference in phase between the two beams increases each time by $\frac{2\pi}{N}$. Each phase shift provides a new fringe pattern, with fringes slightly moving from one case to another. These different fringe patterns are the analogs of the $\tilde{s}^{(i)}$ functions, $i \in \{0, \dots, S-1\}$, represented by the successive horizontal lines in Figure 1-b in the 1D case, and which are obtained with SM by downsampling and interpolation. Taking the argument of the Fourier transform to

retrieve the phase of any pixel of the first fringe pattern obtained by interferometry is equivalent to considering any point M on the first line representing the case $i = 0$ and retrieving the original phase of the 1D signal found along direction t in Figure 1-b, by crossing the different signals obtained with subsequent values of i . No interpolation is performed with classic temporal phase shifting to obtain the successive fringe patterns. Consequently, the argument of the Fourier transform of this set of patterns provides a phase at any pixel, independent from one pixel to another. This is not the case with SM since, with this technique, the phase returned by the procedure is the true phase convolved by the interpolation kernel instead of the true phase, the successive lines being obtained by interpolating sparse experimental data.

4.3 Propagation of sensor noise to displacement maps: displacement resolution

Noise is inherent to data acquisition with digital sensors. Noise transfers to the estimated displacement and limits its resolution. Concerning LSA, a complete discussion of the role of the analysis kernel is available in [45], assuming that image pixels are affected by Gaussian white noise. In this case, displacement maps are affected by a noise field well approximated by a spatially correlated Gaussian noise. Equation 30 shows that ϕ_{SM} is affected by the same additive noise as $\phi_{\text{LSA}}^{f_P}$.

The variance of the noise \tilde{n} in the phase map $\phi_{\text{LSA}}^{f_P}$ is given by the following relation [45]:

$$\text{Var}(\tilde{n}) = \frac{\Delta_x \Delta_y}{2K^2} \|\bar{w}_{\text{MA}}\|^2 \|\bar{w}_{\text{interp}}\|^2 v_{\text{image}} \quad (36)$$

where v_{image} is the variance of the noise affecting the images (caused by sensor noise but also by quantization), $\Delta_x \Delta_y$ is the size of a pixel, K is the modulus of Equation 20, and $\|\cdot\|$ denotes the L^2 norm of a function. The reader is kindly reminded that \bar{w}_{MA} is the normalized moving average kernel along one direction (Section 2.1) and that \bar{w}_{interp} is the normalized interpolation kernel along the orthogonal direction (Section 3.1). Normalized kernels (that is, kernels integrating to 1) are required to obtain Equation 36.

The covariance function of the noise, which characterizes the shape of the noise pattern in the phase maps, is also available in [45].

Concerning the normalized moving average filter \bar{w}_{MA} , one has from Section 2.1, if P is odd:

$$\|\bar{w}_{\text{MA}}^{\text{odd}}\|^2 = \sum_{-(P-1)/2}^{(P-1)/2} \frac{1}{P^2} = \frac{1}{P} \quad (37)$$

and if P is even:

$$\|\bar{w}_{\text{MA}}^{\text{even}}\|^2 = \frac{1}{2P^2} + \sum_{-P/2+1}^{P/2-1} \frac{1}{P^2} = \frac{2P-1}{2P^2} \quad (38)$$

Concerning the interpolation kernel w_{interp} (either linear or cubic in Section 2.2), Appendix A shows that one has either:

$$\|\bar{w}_{\text{interp}}^{\text{lin}}\|^2 = \frac{2}{3S} \quad (39)$$

	linear interpolation	cubic interpolation
odd P	$\frac{\Delta_x \Delta_y}{3SPK^2} v_{\text{image}}$	$\frac{57\Delta_x \Delta_y}{140SPK^2} v_{\text{image}}$
even P	$\frac{(2P-1)\Delta_x \Delta_y}{6SP^2K^2} v_{\text{image}}$	$\frac{57(2P-1)\Delta_x \Delta_y}{280SP^2K^2} v_{\text{image}}$

Table 2: Variance $\text{Var}(\tilde{n})$ of the noise in the phase map retrieved by SM, with a pattern pitch P and a sampling pitch S .

with linear interpolation, or:

$$\|\overline{w}_{\text{interp}}^{\text{cub}}\|^2 = \frac{57}{70S} \quad (40)$$

with cubic interpolation.

Table 2 summarizes the equations of the noise variance in the phase maps retrieved by SM in the four cases studied here.

Finally, an estimation of the standard deviation σ_u of the noise affecting the displacement field is obtained from Equation 1:

$$\sigma_u = \frac{P}{2\pi} \sqrt{\text{Var}(\tilde{n}_{\text{ref}}) + \text{Var}(\tilde{n}_{\text{def}})} = \frac{\sqrt{\omega \mathcal{P} \Delta_x \Delta_y}}{2\pi\sqrt{S}} \sqrt{\frac{1}{K_{\text{ref}}^2} + \frac{1}{K_{\text{def}}^2}} \quad (41)$$

with $\omega = 1/3$ with linear interpolation and $\omega = 57/140$ with cubic interpolation, $\mathcal{P} = P$ with an odd P and $\mathcal{P} = P - 1/2$ with an even P , K_{ref} and K_{def} being the modulus of Equation 20 in the reference and deformed states, respectively.

Since the size of the support of the cubic kernel is larger than that of the linear kernel, we could expect that the noise is smaller in the cubic case, as noisy information is averaged over a larger number of pixels. However, the ω parameter is larger in the cubic case than in the linear case. The noise level also depends on the K_{def} and K_{ref} parameters, which themselves seem to depend on the interpolation kernel and the pattern pitch. It is shown in [44] that these parameters vary slightly around the value $|d_1|\gamma A/2$, where γ is the contrast of the fringe pattern, A is the global illumination level (in Equation 2, $a = A$ and $b = \gamma A/2$), and d_1 is the first coefficient of the Fourier series decomposition of the periodic fringe pattern. The K_{def} and K_{ref} parameters are consequently considered as constant values intrinsic to the fringe pattern; they depend on the pattern pitch but do not depend on the interpolation method. This property was verified experimentally in [33]. We conclude from Equation 41 that, for given pattern and sampling pitches, the ratio between noise level for linear interpolation and noise level for cubic interpolation is $\sqrt{\frac{1/3}{57/140}} \simeq 0.9048$. The noise level is thus larger for cubic interpolation than for linear interpolation. This result is, at first glance, counter-intuitive since a cubic kernel has a larger support than a linear one, but noise propagation also depends on the shape of the kernel.

5 Numerical simulations

This section aims to verify the theoretical predictions of Section 4 on the displacement maps retrieved by SM, in terms of both the attenuation of the amplitude of the displacement and noise propagation. Pairs of synthetic noiseless and noisy reference and deformed images were considered for this comparison. We first briefly explain how these synthetic images were obtained and justify the choice of the reference displacement field used to deform the reference image. This displacement field then serves as a ground-truth reference to assess the quality of the displacement field returned by SM with different settings. Two points are examined here in turn: *i*- the theoretical prediction of the attenuation of the displacement as a function of the spatial frequency, and *ii*- the propagation of image noise to the final displacement field returned by SM and given by Equation 41. The attenuation in Point *i*- is the displacement bias studied in [11] for LSA, and the standard deviation of the noise affecting the displacement maps is also referred to as the displacement resolution [1, 4].

Software programs to reproduce the numerical simulations are freely available at the following URL:

<https://members.loria.fr/FSur/software/resolutionSM/>

5.1 Synthetic image rendering program

The synthetic images of a 2D grid with lines aligned along the horizontal and vertical directions were obtained with 2DGridRender. This program was developed to render images of undeformed and deformed periodic patterns. It is a simple adaptation of BSpeckleRender introduced in [43] to render random speckles suitable for DIC. This program is available online¹. The reference displacement field being given, the main benefit of this program is that the image of the deformed configuration is not affected by interpolation bias. Fifteen sampling densities of the periodic pattern were considered, the pattern pitch being chosen in such a way that $P \in \{6, 6.5, 7, 10, 10.5, 11, 14, 14.5, 15, 18, 18.5, 19, 22, 22.5, 23\}$ [px]. Note that P takes odd and even values, which requires using w_{MA}^{odd} or w_{MA}^{even} . Grids with non-integer values are processed using the moving average filter that would be used with the rounded value of P (thus w_{MA}^{odd} here). Consequently, these 2D grids give 1D fringes in which the influence of the orthogonal 1D fringes is not properly discarded, especially for small values of P , the relative difference between P and its rounded value being larger in this case.

As explained in [43], the image in the reference state is the image of the deformed grid, and the image in the deformed state is the image of the non-deformed grid, so that the output of SM can be compared with the ground-truth reference displacement field instead of the inverse displacement field.

5.2 Ground-truth reference displacement field

The idea here is to deform a synthetic 2D grid through a controlled displacement field. The 2D grid images are 2000×501 pixels in size for the fifteen sampling densities considered in this

¹<https://members.loria.fr/FSur/software/BSpeckleRender/>

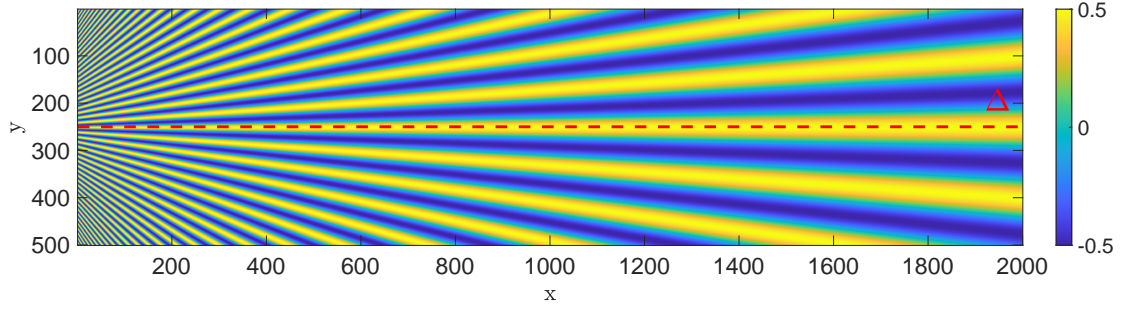


Figure 3: Reference vertical displacement field u_y ($u_x = 0$). Throughout the paper, the cross-section of the different u_2 displacement fields will be given along the midline Δ .

study. The reference displacement field chosen here is null along the horizontal axis x . Along the vertical direction y , this is a sine wave featuring a period gently linearly decreasing from the left to the right, see Figure 3. The minimum value of the period of the wave is equal to twice the period P of the 2D grid, and the maximum value to a quantity that depends on the sampling density because the size of the images remains the same for all values of P .

This reference displacement field has already been employed in previous studies dealing with the metrological performance of full-field measurement techniques, see [3, 11, 14, 34, 3, 51]. It was christened the “STAR” displacement field in [34]. Processing a pair of reference and deformed images deformed through this reference displacement field enables us to quantify the actual progressive attenuation of the amplitude of the sine wave modeling the u_y displacement when going to the left of the field, thus to the highest frequencies. This is a direct effect of the convolution of the actual displacement field by a triangular or a cubic kernel, as claimed in Section 4.2 above.

5.3 Setting the parameters governing sampling moiré

The synthetic images were processed following the same methodology as that discussed in Section 5.1. The sampling pitch S was chosen to be equal to $S = P - 1$, P being the period of the two 1D grids, but other integer values smaller than but close to P can potentially be chosen. Two interpolation methods were considered: linear and cubic.

Note finally that, as proposed in [47] and in line with Equation 8, the two phase distributions $\Phi_i, i \in \{x, y\}$ were extracted pixelwise from the S successive fringe patterns by using the following equation:

$$\Phi_i(x, y) = -\arctan \left(\frac{\sum_{k=0}^{S-1} \tilde{s}_i^{(k)}(x, y) \sin(2k\pi/S)}{\sum_{k=0}^{S-1} \tilde{s}_i^{(k)}(x, y) \cos(2k\pi/S)} \right), \quad i \in \{x, y\}, \quad (42)$$

where $\tilde{s}_i^{(k)}$ denotes the k th alias along direction i , $i \in \{x, y\}$, and \arctan the four-quadrant inverse tangent function.

5.4 Simulation #1: bias in SM caused by the attenuation of the displacement field

The first simulation deals with the attenuation of the spatial frequencies involved in the displacement to be measured. The main steps of the SM procedure are first briefly illustrated in Figures 4-(a) to (g) successively show a close-up view of:

- The 2D grid in the case $P = 11$ [px] (-a).
- The two 1D grids obtained after convolving the 2D grid with the moving average kernel w_{MA}^{odd} , as described in Section 2.1, along the x (b) and y (c) directions.
- Two typical successive fringe patterns along x ((d)-(f)) and y ((e)-(g)) retrieved after downsampling and interpolation.
- u_x (h) and u_y (i) found at the end of the procedure.

A difference between the reference vertical displacement field and its counterpart returned by SM can be observed by comparing the maps shown in Figures 4-(i) and 3, especially for the highest spatial frequencies (on the left of the displacement field). The same remark holds with u_x , for which the reference displacement is null. This attenuation of the u_y displacement becomes clearer when plotting the cross-section of the u_y displacement map along the midline (denoted by Δ in Figure 3). The same cases as above are considered: linear and cubic interpolations, and $P \in \{6, 6.5, 7, 10, 10.5, 11, 14, 14.5, 15, 18, 18.5, 19, 22, 22.5, 23\}$ [px]. The curves obtained with these different settings are reported in Figure 5, subfigures (a) and (b) showing the results for linear and cubic interpolation, respectively. The curve given by the theoretical prediction in Equation 35 is also superposed in each case for comparison purposes. In this latter equation, w_{SM} is built upon $w_{MA} = w_{MA}^{even}$ or w_{MA}^{odd} , depending on the parity of P (or of the rounded value of P), and upon $w_{interp} = w_{interp}^{lin}$ or w_{interp}^{cub} , depending on the interpolation scheme.

Several lessons can be drawn from Figure 5. One can see that the displacement retrieved by SM with linear interpolation is lower than the one obtained with cubic interpolation. This means that, all other things being equal, cubic interpolation gives a lower (thus better) measurement bias. Besides, the general shape of the curves given by the output of SM and the predicted curves are alike. More precisely, the measurement bias is correctly estimated for linear interpolation, and also for cubic interpolation when the pattern pitch (or the sampling density) is significant. This validates the proposed predictive formula. However, some differences can be seen. Both in the linear and the cubic interpolation cases, one can see, in the case of a pixel density larger than 18 pixels per period, that high-frequency displacements (left-hand side of the curves) are not correctly retrieved by SM, with a quite different estimation from the predicted displacement. The reason is probably that the approximation of Equation 7 is too coarse, the sampling frequency being too low to interpolate the SM fringe with an accuracy sufficient to correctly represent the high-frequency displacement. Another difference is that the retrieved displacements generally slightly undermatch the predicted ones. Several factors explain these differences. First, Equation 30 is valid under the linear-phase assumption. While ϕ_{LSA} is shown to be well approximated by the convolution product between the kernel and the true phase under the less restrictive small strain assumption, Equation 30 may not give an accurate equality.

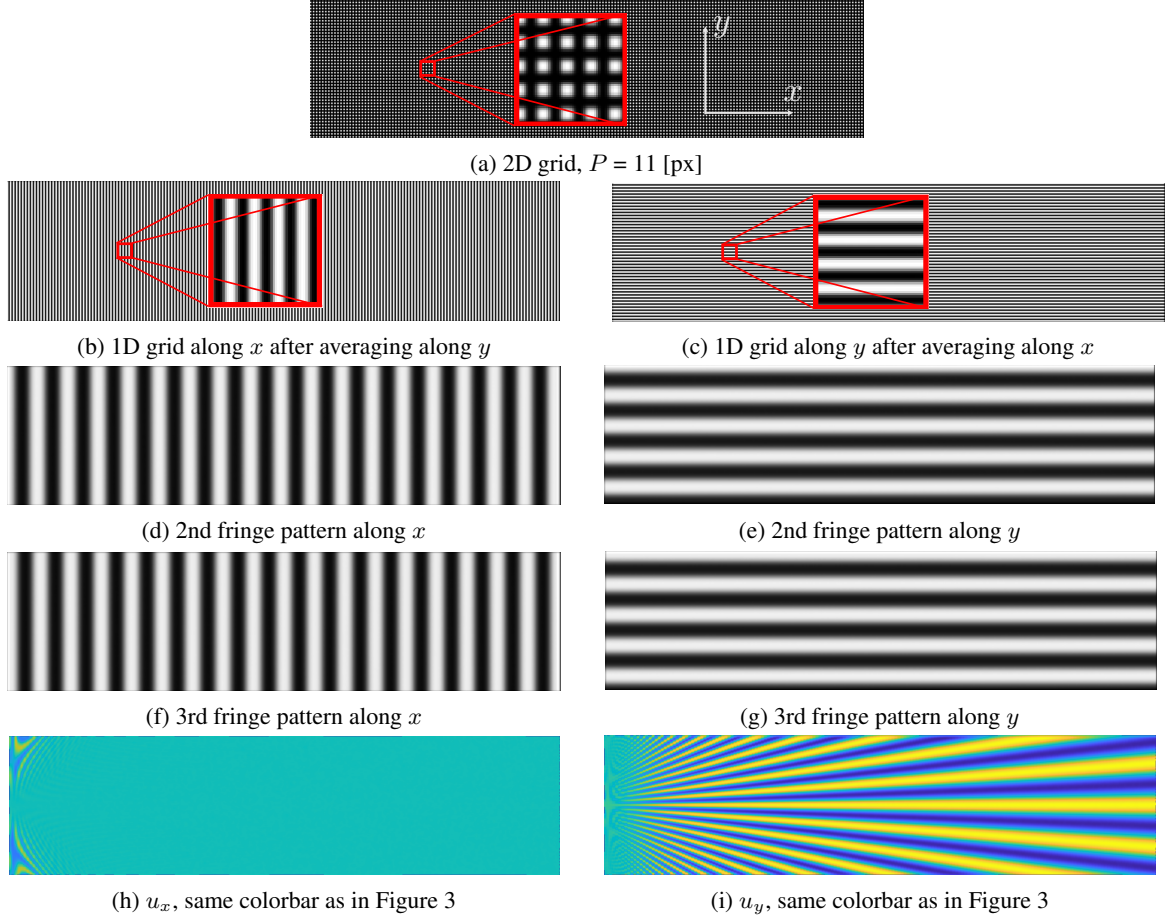
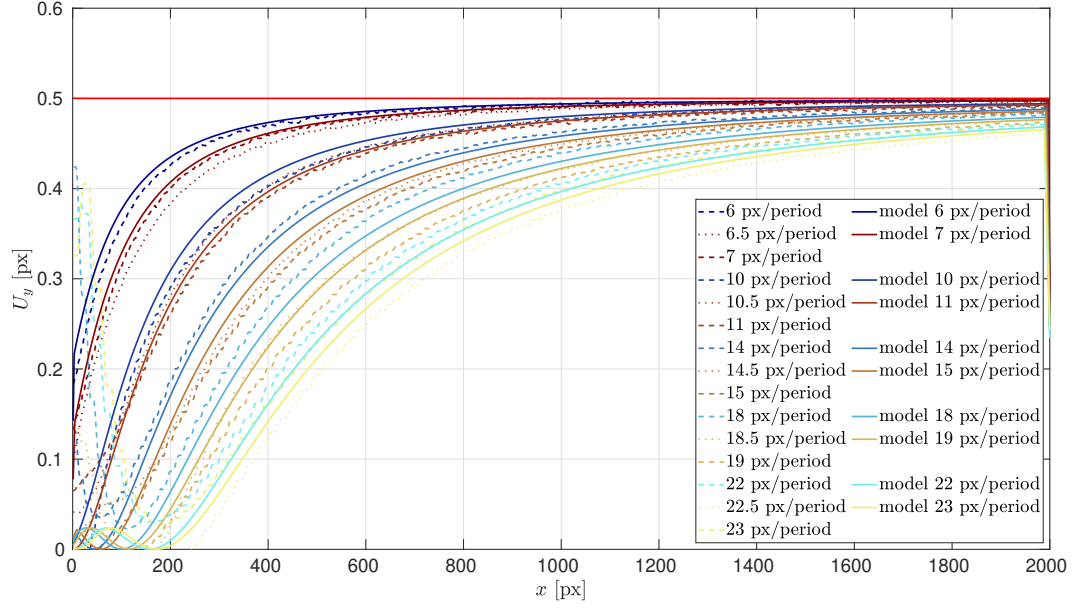


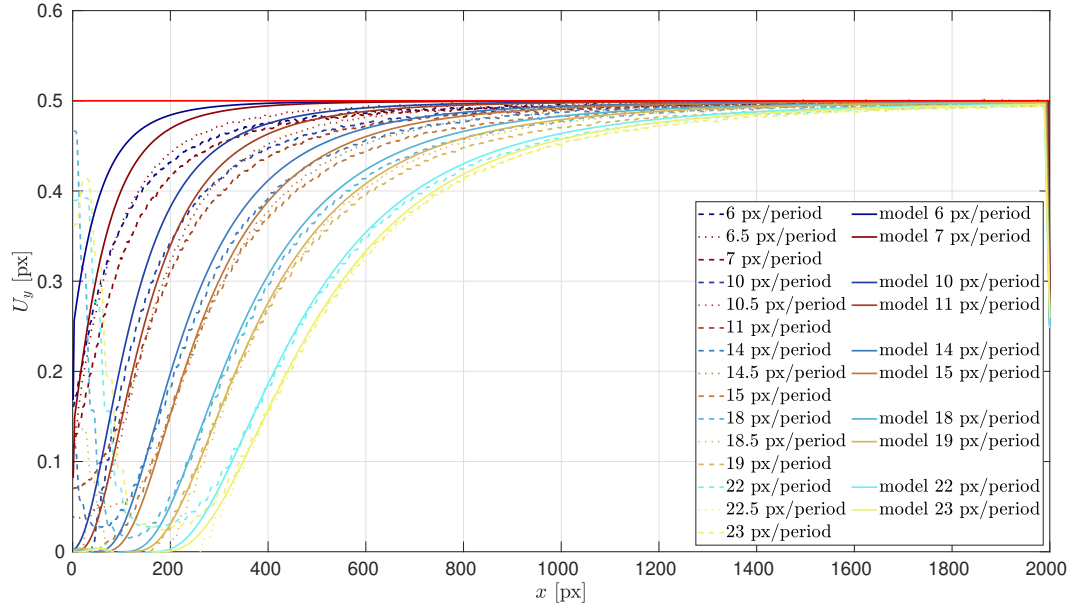
Figure 4: Illustration of the different steps of SM in a typical case. (a): 2D grid with pitch $P = 11$ [px], (b): 1D grid obtained by applying a vertical mean filter of length $P = 11$ [px], (c): 1D grid obtained by applying a horizontal mean filter of length $P = 11$ [px], (d)(f): two successive fringe patterns obtained after downsampling with a period $S = P - 1 = 10$ [px] and cubic interpolation. A one-pixel shift is applied rightwards from one case to another, see Figure 1-(a). (e)(g): two successive fringe patterns obtained after downsampling and cubic interpolation. A one-pixel shift is applied downwards from one case to the other. (h)(i): u_x and u_y displacement fields retrieved by SM (same colorbar as in Figure 3).

Second, and probably more importantly, grids are not pure sine functions. Real grids are indeed the superposition of harmonics of the pitch frequency f_P . It is shown in [45] that the influence of these harmonics is not suppressed by using triangular or rectangular windows in windowed Fourier analysis. This gives spurious displacement estimations, contrary to the Gaussian window used in LSA and WFR.

Concerning non-integer pitches P , one can see that using the moving average filter w_{MA} parameterized by the rounded value of P gives curves below the curve for the nearest odd value and above the curve for the nearest even value, except for the smallest values of P . The pre-



(a) Linear interpolation



(b) Cubic interpolation

Figure 5: Cross-section along line Δ (defined in Figure 3) of the displacement u_y obtained for various settings: linear and cubic interpolations, $P \in \{6, 6.5, 7, 10, 10.5, 11, 14, 14.5, 15, 18, 18.5, 19, 22, 22.5, 23\}$ [px]. The red plain line is the ground-truth value, the dashed and dotted lines are the output of SM (dashed for integer P and dotted for non-integer P), and the plain lines (model) are the displacement predicted by Equation 35. The output of SM has to be compared with the corresponding predicted curve.

dictive formula is thus still valid with non-integer pitches, despite grids processed by w_{MA} yield 1D fringes with residual components of the orthogonal fringes. As P increases, the curves for non-integer P get closer to the corresponding curves with an odd P , as the residuals become smaller.

5.5 Simulation #2: sensor noise propagation to the displacement maps in SM

The propagation of sensor noise to the final displacement maps is examined here. The objective is to compare the value given by the theoretical prediction of the standard deviation of the displacement noise given by Equation 41, and the standard deviation estimated from simulated data.

We consider here the same 2D grid as that depicted in Figure 4-(a). A Gaussian white noise of standard deviation $\sigma_{image} = 2.5$ [gray level] is added before quantization to the synthetic images of the reference and deformed configurations. This is a common and realistic value for camera sensors featuring a gray depth equal to 8 bits, giving a pixel intensity between 0 and 255 [gray level]. Strictly speaking, sensor noise is a mixture of Poisson and Gaussian processes, but a transform as the generalized Anscombe transform [42] reduces the noise to a Gaussian white noise as assumed here. The standard deviation of the noise affecting the displacement field retrieved with SM from synthetic noisy images is denoted by $\sigma_{u_i}^{sim}$, $i \in \{x, y\}$, while their counterparts deduced from Equation 41 are denoted by $\sigma_{u_i}^{pred}$, $i \in \{x, y\}$.

The values of $\sigma_{u_x}^{sim}$ and $\sigma_{u_y}^{sim}$ are estimated by subtracting the displacement fields obtained from $N = 100$ noisy images on the one hand and from the noiseless image on the other hand, by calculating the variance at each pixel of the distribution of the N resulting noise samples, by averaging this variance over the resulting field, and by eventually taking the square root of the result.

The standard deviation $\sigma_{u_i}^{pred}$ of the noise in the u_i displacement field, $i \in \{x, y\}$, is obtained with Equation 41, with ω and \mathcal{P} set in line with the parity of P and the interpolation scheme.

For the grid depicted in Figure 4-(a), the quantities involved in the latter equation are estimated as follows:

- The unit being the pixel for the lengths, we have $\Delta_x = \Delta_y = 1$ [px].
- The variance v_{image} of image noise is equal to $v_{image} = \sigma_{image}^2 = 2.5^2$ [(gray level)²].
- The same ten values for the pitch P as in Section 5.4 above were considered ($P \in \{6, 7, 10, 11, 14, 15, 18, 19, 22, 23\}$ [px]), and the sampling pitch was equal to $S = P - 1$.
- The modulus of each windowed Fourier transform K_i^{ref} and K_i^{def} was obtained numerically with a Matlab code for both the reference and the deformed images: the norm of the Fourier transform was computed, then averaged over the whole maps to obtain estimations of K_i^{ref} and K_i^{def} .

Figure 6 gives the estimation of K_i^{ref} and K_i^{def} , $i \in \{x, y\}$, which are nearly superposed. As predicted in Section 4.3, only the pattern pitch has an influence. One can see that the larger the pitch, the larger K_i^{ref} and K_i^{def} . This was also seen in real experiments and discussed in [33]:

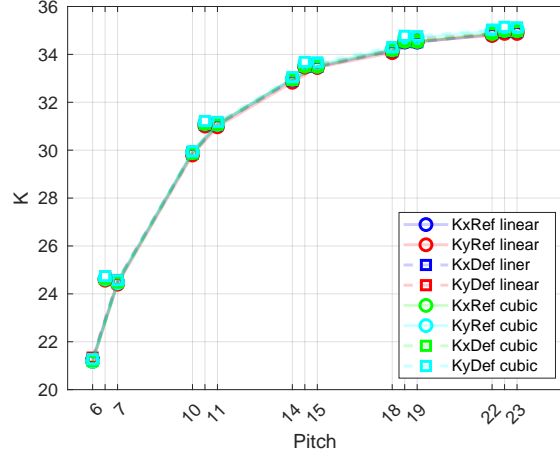


Figure 6: K_i^{ref} and K_i^{def} ($i = x, y$) as a function of the number of pixels per period, with linear and cubic interpolation. For better readability, values for non-integer pitches are not connected to other values.

images with large pattern pitches show higher contrast γ (while small pitches give blurred details when reaching the pixel scale), thus higher K values as mentioned in Section 4.3. One can also see that values of K for non-integer pitches are slightly off the trend.

To illustrate noise affecting displacement fields, Figure 7 shows the difference between u_y obtained from a noise-free image (as in Figure 4) and u_y obtained from a noisy image. The close-up view shows a correlated noise, characterized in [45]. It is worth noting that the “blobs” represented in this figure are elongated along y . This is because the corresponding kernel is also elongated along direction y for this calculation.

Figure 8(a) shows the predicted $\sigma_{u_i}^{\text{pred}}$ noise level in the x - and y - displacement maps for linear and cubic interpolation. No difference can be observed between these two directions, the corresponding curves being nearly superposed. Cubic interpolation yields a larger noise than linear interpolation. The ratio between the predicted noise level in the linear and cubic cases is 0.9048 in both directions and for any value of the number of pixels per period, as predicted in Section 4.3. In both cases, increasing the number of pixels per period causes the noise level to decrease. Figure 8(b) shows the $\sigma_{u_i}^{\text{sim}}$ noise level evaluated on simulated data. The same observations apply. Figure 8(c) shows the ratio between $\sigma_{u_i}^{\text{pred}}$ and $\sigma_{u_i}^{\text{sim}}$, which is close to 1. We can see a larger difference when linear interpolation is used, but the standard deviation is generally predicted with a relative accuracy smaller than 1. Non-integer pitches systematically give a smaller noise level than expected, which is caused by the fact that the moving average filter, parameterized by the rounded value of the pitch, is here larger than needed. Despite transforming 2D grids in 1D fringe patterns should probably be achieved through a dedicated filter, the simple moving average filter used here gives consistent results.

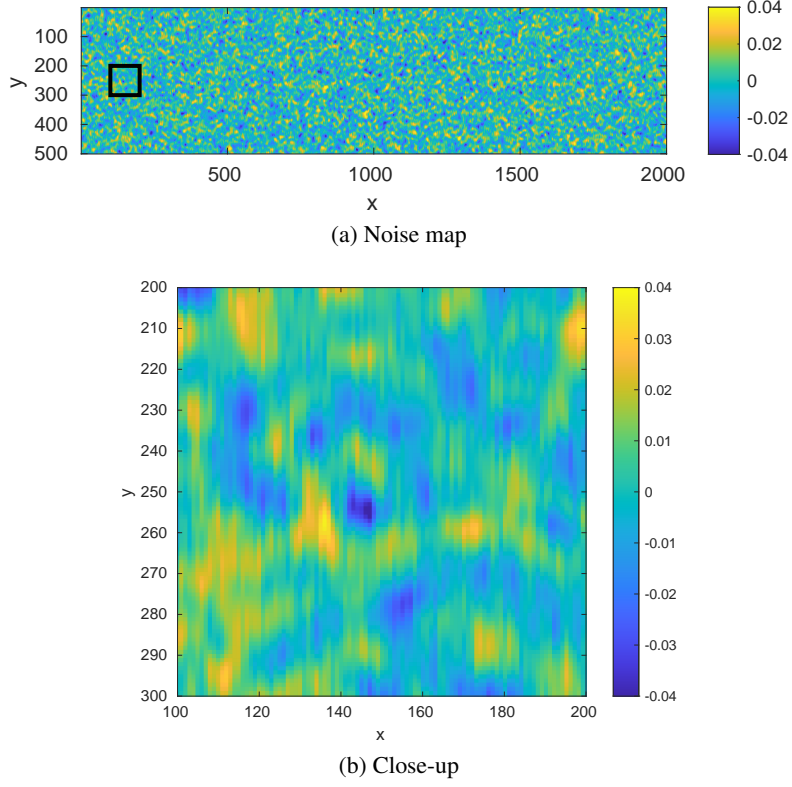


Figure 7: (a) Difference between u_y obtained from a pair of noise-free images (as in Figure 4) and u_y obtained from a pair of noisy images. (b) Close-up view on the region marked by a black rectangle in (a).

6 Conclusion

The link between two techniques aimed at processing images of periodic patterns to extract displacement fields under the small strain hypothesis, namely Localized Spectrum Analysis (LSA) and Sampling Moiré (SM), was established in this paper. As already discussed in previous studies of the optical metrology literature, it was demonstrated here, but in a different way, that the latter is a particular case of the former. We relied here on the fact that interpolation performed in SM can be interpreted as a convolution with specific kernels. Predictive formulas for some parameters characterizing the metrological parameters of LSA being available and validated in the literature, we explored then their applicability to SM. Numerical experiments show that the measurement bias is correctly estimated for linear interpolation, and that it is as correctly estimated, in the cubic interpolation case, if the sampling density of the images is high. Concerning the measurement resolution, it is shown that predictive formulas derived from LSA are accurate for SM. As far as the interpolation scheme in SM is concerned, one of the findings of this study is that cubic interpolation gives a lower (thus better) measurement bias than linear interpolation but also gives a larger (thus worse) measurement resolution.

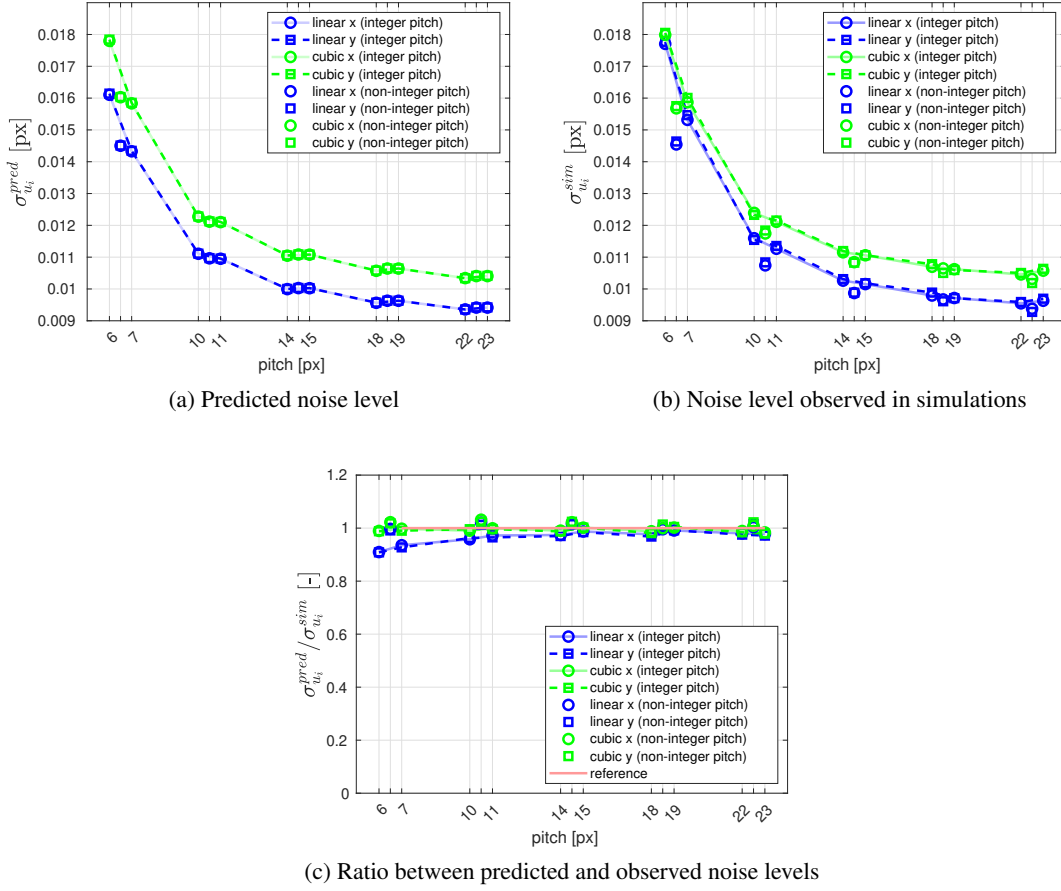


Figure 8: (a) Predicted standard deviation $\sigma_{u_i}^{\text{pred}}$. (b) Standard deviation $\sigma_{u_i}^{\text{sim}}$ estimated on simulated data. (c) $\sigma_{u_i}^{\text{pred}} / \sigma_{u_i}^{\text{sim}}$ ratio.

A Calculations for Equations 39 and 40

We approximate the discrete sum with an integral to retrieve simpler closed-form expression, as in [45].

With linear interpolation:

$$\|\bar{w}_{\text{interp}}^{\text{lin}}\|^2 = 2\kappa^2 \int_0^S \left(1 - \frac{x}{S}\right)^2 dx = \frac{2\kappa^2 S}{3} \quad (43)$$

where $1/\kappa = \int_{-S}^S k(x)dx = 2S \int_0^1 (1-x)dx = S$.

This gives Equation 39.

With cubic interpolation (not addressed in [45]):

$$\begin{aligned} \|\bar{w}_{\text{interp}}^{\text{lin}}\|^2 &= 2\kappa^2 \left(\int_0^S \left(\frac{3}{2} \left(\frac{x}{S} \right)^3 - \frac{5}{2} \left(\frac{x}{S} \right)^2 + 1 \right)^2 dx \right. \\ &\quad \left. + \int_S^{2S} \left(-\frac{1}{2} \left(\frac{x}{S} \right)^3 + \frac{5}{2} \left(\frac{x}{S} \right)^2 - 4 \left(\frac{x}{S} \right) + 2 \right)^2 dx \right) \end{aligned} \quad (44)$$

$$= 2\kappa^2 S \left(\int_0^1 \left(\frac{3}{2} x^3 - \frac{5}{2} x^2 + 1 \right)^2 dx + \int_1^2 \left(-\frac{1}{2} x^3 + \frac{5}{2} x^2 - 4x + 2 \right)^2 dx \right) \quad (45)$$

$$= 2\kappa^2 S (17/42 + 1/420) = \frac{57\kappa^2 S}{70} \quad (46)$$

where $1/\kappa = \int_{-2S}^{2S} k(x) dx = 2S \left(\int_0^1 \left(\frac{3}{2} x^3 - \frac{5}{2} x^2 + 1 \right) dx + \int_1^2 \left(-\frac{1}{2} x^3 + \frac{5}{2} x^2 - 4x + 2 \right) dx \right) = 2S(13/24 - 1/24) = S$.

This gives Equation 40.

References

- [1] International vocabulary of metrology. Basic and general concepts and associated terms, 2008. Third edition.
- [2] G.F. Bomarito, J.D. Hochhalter, T.J. Ruggles, and A.H. Cannon. Increasing accuracy and precision of digital image correlation through pattern optimization. *Optics and Lasers in Engineering*, 91:73–85, 2017.
- [3] B. Chen and S. Coppieters. Meshfree digital image correlation using element free Galerkin method: Theory, algorithm and validation. *Experimental Mechanics*, 63(3):517–528, 2023.
- [4] A. Chrysochoos and Y. Surrél. Basics of metrology and introduction to techniques. In M. Grédiac and F. Hild, editors, *Full-field measurements and identification in solid mechanics*, chapter 1, pages 1–29. Wiley, 2012.
- [5] K. Creath. Phase-measurement interferometry techniques. In E. Wolf, editor, *Progress in Optics*, volume 26, pages 349–393. Elsevier, 1988.
- [6] X. Dai, H. Xie, and H. Wang. Geometric phase analysis based on the windowed Fourier transform for the deformation field measurement. *Optics and Laser Technology*, 58(6):119–127, 2014.
- [7] X. Dai, H. Xie, H. Wang, C. Li, Z. Liu, and L. Wu. The geometric phase analysis method based on the local high resolution discrete Fourier transform for deformation measurement. *Measurement Science and Technology*, 25(2):025402, 2014.

- [8] P. Getreuer. Linear methods for image interpolation. *Image Processing On Line*, 1:238–259, 2011.
- [9] D. C. Ghiglia and M. D. Pritt. *Two-Dimensional Phase Unwrapping: Theory, Algorithms, and Software*. Wiley, 1998.
- [10] M. Grédiac, X. Balandraud, B. Blaysat, T. Jailin, R. Langlois, F. Sur, and A. Vinel. Fine-tuning a deconvolution algorithm to restore displacement and strain maps obtained with LSA. *Experimental Mechanics*, 63(9):1509–1537, 2023.
- [11] M. Grédiac, B. Blaysat, and F. Sur. A critical comparison of some metrological parameters characterizing local digital image correlation and grid method. *Experimental Mechanics*, 57(6):871–903, 2017.
- [12] M. Grédiac, B. Blaysat, and F. Sur. Extracting displacement and strain fields from checkerboard images with the localized spectrum analysis. *Experimental Mechanics*, 59(2):207–218, 2019.
- [13] M. Grédiac, B. Blaysat, and F. Sur. A robust-to-noise deconvolution algorithm to enhance displacement and strain maps obtained with local DIC and LSA. *Experimental Mechanics*, 59(2):219–243, 2019.
- [14] M. Grédiac, B. Blaysat, and F. Sur. On the optimal pattern for displacement field measurement: random speckle and DIC, or checkerboard and LSA? *Experimental Mechanics*, 60(4):509–534, 2020.
- [15] M. Grédiac, F. Sur, and B. Blaysat. The grid method for in-plane displacement and strain measurement: a review and analysis. *Strain*, 52(3):205–243, 2016.
- [16] M. Grédiac, F. Sur, and B. Blaysat. Comparing several spectral methods used to extract displacement and strain fields from checkerboard images. *Optics and Lasers in Engineering*, 127:105984, 2020.
- [17] J.E. Greivenkamp and J.H. Bruning. Phase shifting interferometers. In D. Malacara, editor, *Optical shop testing, 2nd edition*, chapter 14, pages 501–598. Wiley, 1992.
- [18] M. Arevallilo Herráez, D.R. Burton, M.J. Lalor, and M.A. Gdeisat. Fast two-dimensional phase-unwrapping algorithm based on sorting by reliability following a noncontinuous path. *Applied Optics*, 41(35):7437–7444, 2002.
- [19] M. J. Hÿtch and T. Plamann. Imaging conditions for reliable measurement of displacement and strain from high-resolution electron microscope images. *Ultramicroscopy*, 87:199–212, 2001.
- [20] M. J. Hÿtch, E. Snoeck, and R. Kilaas. Quantitative measurement of displacement and strain fields from HREM micrographs. *Ultramicroscopy*, 74:131–146, 1998.
- [21] M.F. Kasim. Fast 2D phase unwrapping implementation in MATLAB, 2017. https://github.com/mfkasim91/unwrap_phase/.

- [22] Q. Kemao. Windowed fourier transform for fringe pattern analysis. *Applied Optics*, 43(13):2695–2702, 2004.
- [23] Q. Kemao. *Windowed Fringe Pattern Analysis*. SPIE Press, 2013.
- [24] Q. Kemao. Applications of windowed Fourier fringe analysis in optical measurement: A review. *Optics and Lasers in Engineering*, 66:67–73, 2015.
- [25] Q. Kemao. Carrier fringe pattern analysis: Links between methods. *Optics and Lasers in Engineering*, 150:106874, 2022.
- [26] Q. Kemao, N. Agarwal, S. Ri, and Q. Wang. Sampling moiré as a special windowed Fourier ridges algorithm in demodulation of carrier fringe patterns. *Optical Engineering*, 57(10):100503, 2018.
- [27] R. Keys. Cubic convolution interpolation for digital image processing. *IEEE Transactions on Acoustics, Speech, and Signal Processing*, 29(6):1153–1160, 1981.
- [28] Y. Li and H. Xie. Identification of thermomechanical parameters based on the virtual fields method combined with the sampling moiré method. *Strain*, 59(1):e12429, 2023.
- [29] R. J. Marks. *Introduction to Shannon sampling and interpolation theory*. Springer, 2012.
- [30] Y. Morimoto and M. Fujigaki. Theory and application of sampling moiré method. In *Selected Papers from the Symposium on Recent Advances in Mechanics*, pages 227–248. Springer Netherlands, 2011.
- [31] B. Pan, K. Qian, H. Xie, and A. Asundi. Two-dimensional digital image correlation for in-plane displacement and strain measurement: a review. *Measurement Science and Technology*, 20(6):062001, 2009.
- [32] M. Pirga and M. Kujawinska. Two directional spatial-carrier phase-shifting method for analysis of crossed and closed fringe patterns. *Optical Engineering*, 34(8):2459 – 2466, 1995.
- [33] S. Qin, M. Grédiac, B. Blaysat, S. Ma, and F. Sur. Influence of the sampling density on the noise level in displacement and strain maps obtained by processing periodic patterns. *Measurement*, 173:108570, 2021.
- [34] P. L. Reu, B. Blaysat, E. Andó, K. Bhattacharya, C. Couture, V. Couty, D. Deb, S. S. Fayad, M. A. Iadicola, S. Jaminion, M. Klein, A. K. Landauer, P. Lava, M. Liu, L. K. Luan, S. N. Olufsen, J. Réthoré, E. Roubin, D. T. Seidl, T. Siebert, O. Stamati, E. Toussaint, D. Turner, C. S. R. Vemulapati, T. Weikert, J. F. Witz, O. Witzel, and J. Yang. DIC challenge 2.0: developing images and guidelines for evaluating accuracy and resolution of 2D analyses. *Experimental Mechanics*, 62(1):639—654, 2022.
- [35] S. Ri, N. Agarwal, Q. Wang, and Q. Kemao. Comparative study of sampling moiré and windowed Fourier transform techniques for demodulation of a single-fringe pattern. *Applied Optics*, 57(36):10402–10411, 2018.

- [36] S. Ri, M. Fujigaki, and Y. Morimoto. Sampling moiré method for accurate small deformation distribution measurement. *Experimental Mechanics*, 50(4):501–508, 2010.
- [37] S. Ri and T. Muramatsu. Theoretical error analysis of the sampling moiré method and phase compensation methodology for single-shot phase analysis. *Applied Optics*, 51(16):3214–3223, 2012.
- [38] S. Ri, T. Muramatsu, M. Saka, K. Nanbara, and D. Kobayashi. Accuracy of the sampling moiré method and its application to deflection measurements of large-scale structures. *Experimental Mechanics*, 52(4):331–340, 2012.
- [39] H. Schreiber and J. H. Bruning. *Phase Shifting Interferometry*, chapter 14, pages 547–666. Wiley, 2007.
- [40] H. Schreier, J.J. Orteu, and M.A. Sutton. *Image correlation for shape, motion and deformation measurements: Basic concepts, theory and applications*. Springer, 2009.
- [41] M. Servin, J. A. Quiroga, and J. M. Padilla. *Fringe Pattern Analysis for Optical Metrology*. John Wiley & Sons, Ltd, 2014.
- [42] J.-L. Starck, F.D. Murtagh, and A. Bijaoui. *Image Processing and Data Analysis*. Cambridge University Press, 1998.
- [43] F. Sur, B. Blaysat, and M. Grédiac. Rendering deformed speckle images with a Boolean model. *Journal of Mathematical Imaging and Vision*, 60(5):634–650, 2018.
- [44] F. Sur and M. Grédiac. Towards deconvolution to enhance the grid method for in-plane strain measurement. *AIMS Inverse Problems and Imaging*, 8(1):259–291, 2014.
- [45] F. Sur and M. Grédiac. Influence of the analysis window on the metrological performance of the grid method. *Journal of Mathematical Imaging and Vision*, 56(3):472–498, 2016.
- [46] M. Takeda, H. Ina, and S. Kobayashi. Fourier-transform method of fringe-pattern analysis for computer-based topography and interferometry. *Journal of the Optical Society of America*, 72(1):156–160, 1982.
- [47] Q. Wang and S. Ri. Sampling moiré method for full-field deformation measurement: A brief review. *Theoretical and Applied Mechanics Letters*, 12(1):100327, 2022.
- [48] Q. Wang, S. Ri, and T. Enomoto. Residual thermal strain distribution measurement of underfills in flip chip electronic packages by an inverse approach based on the sampling moiré method. *Experimental Mechanics*, 60(5):611–626, 2020.
- [49] Q. Wang, S. Ri, M.J.M. Fikry, and S. Ogihara. Multiplication sampling moiré method for full-field deformation measurement of composite materials. *Optical Letters*, 47(1):70–73, 2022.

- [50] Q. Wang, S. Ri, H. Tsuda, M. Koyama, and K. Tsuzaki. Two-dimensional moiré phase analysis for accurate strain distribution measurement and application in crack prediction. *Optics Express*, 25(12):13465–13480, 2017.
- [51] Y. Wang and J. Zhao. DIC-Net: Upgrade the performance of traditional DIC with Hermite dataset and convolution neural network. *Optics and Lasers in Engineering*, 160:107278, 2023.
- [52] L. Wittevrongel, P. Lava, S.V. Lomov, and D. Debruyne. A self adaptive global digital image correlation algorithm. *Experimental Mechanics*, 55(2):361–378, 2015.